國立交通大學

電子物理研究所

碩士論文

氮化銦奈米點受覆蓋層影響之研究

Studies of capping effects on InN nano-dots

研 究 生：邱泰鑫

指導教授：李明知 教授

中華民國九十五年七月

氮化銦奈米點受覆蓋層影響之研究

Studies of capping effects on InN nano-dots

研 究 生：邱泰鑫　　Student: Tai-Hsin Chiu

指導教授：李明知 教授　　Advisor: Prof. Ming-Chih Lee

A Thesis
Submitted to Institute of Electrophysics
College of Science
National Chiao Tung University
in Partial Fulfillment of the Requirements
for The Degree of Master of Physics
in
Electrophysics
July 2006
Hsinchu, Taiwan, Republic of China

中華民國九十五年七月

Acknowledgment

研究所兩年的求學時光真的過得好快，回憶這兩年，雖然很累卻也是最充實收穫最多的一段日子。很榮幸能成為交大的一份子，也很感謝學校以及 Raman 實驗室所提供的豐沛資源。

在研究方面，要感謝李明知老師、張文豪老師、陳衛國老師與周武清老師的悉心教導。其中，特別感謝我的指導教授李明知老師在研究方向、實驗過程以及論文寫作上的教導與建議，因有您的耐心教導以及寶貴的建議才使得我能順利完成論文研究。此外，要感謝博班學長：古慶順、柯文政、李寧、陳京玉、蔡仪哲、傅振邦等在實驗研究上的教導及建議。特別要感謝古慶順學長在實驗及研究上的耐心教導，因有您的帶領及指導才使我能順利完成研究；以及柯文政學長提供合適的樣品。同時更感謝實驗室同學：維偲、士傑、士凱、啟仁、家禎、尚樺；學長姐：碧軒、信志、鐘逸、逸文、承勳、佳進；以及學弟妹：少甫、沛雯、書鴻、仲葳、進吉、峰毅。因有你們的陪伴，與分享課業及生活上的點點滴滴，使我這兩年的研究所生活更加多采多姿，真的很感謝你們帶給我的這段美好回憶。

最後，感謝我的父母及家人，因有你們的辛勤付出與支持才使得我能專心完成這段學業及論文。

泰鑫 於新竹交大 95.7

Index

氮化銦奈米點受覆蓋層影響之研究

研究生：邱泰鑫　　指導教授：李明知 博士

國立交通大學

電子物理研究所

中文摘要

在本論文中，我們研究氮化銦奈米點在長晶過程中加上覆蓋層對其在表面形貌，組成變化，以及光學特性方面的影響。此氮化銦奈米點樣本是以流率中斷法於有機金屬氣相磊晶系統中所成長。我們藉由原子力顯微鏡系統探討氮化銦奈米點表面形貌變化。由原子力顯微鏡影像所顯示，當未有覆蓋層時，氮化銦類圓盤狀奈米點結構所呈現的平均密度為 3.9×10^{8} cm^{-2}以及平均高度為 24.3nm。隨著覆蓋層溫度增加時，氮化銦奈米點的形狀開始改變以及平均密度也隨之降低。其相似的趨勢也在螢光光譜上被觀察到。螢光光譜量測所示，氮化銦奈米點發光位置約在 0.77eV。這與最近文獻上所提到的結果是相符合的。此外，對於氮化銦奈米點螢光強度隨著覆蓋層溫度增加的變化趨勢，與由原子力顯微鏡影像所呈現的結果是一致的。此

外，另有兩個強度很明顯的可見光螢光訊號被觀察到。其位置分別落於2.975eV(紫光)以及 2.37eV(綠光)。藉由高繞射角X光繞射光譜的分析，我們發先有兩個譜峰位置分別在 71.7°及 70.2°。比對螢光光譜和X光繞射光譜的關係，我們發現這個變化明顯地是由覆蓋層所影響而且推測那兩個可見光螢光訊號可能是來自於氮化鎵銦的組成變化。此外，其他的成因也不能完全排除,例如深層能階的缺陷態。我們進一步由近場光學顯微系統分析此螢光訊號的空間對應關係，並且也提出我們的解釋，此螢光訊號是來自於覆蓋層以及氮化銦奈米點與氮化鎵緩衝層間的中間層。

Studies of capping effects on InN nano-dots

Student: Tai-Hsin Chiu Advisor: Dr. Ming-Chih Lee

Institute of Electrophysics

National Chiao Tung University

Abstract

In this study, we investigated the capping effects on InN nano-dots which were grown by flow-rate-interruption method using metal organic chemical vapor deposition (MOCVD) in terms of morphology, composition, and optical properties aspect. The InN nano-dots morphology was examined by atomic force microscopy (AFM). AFM images showed the disk-like dots with average density of 3.9×10^{8} cm^{-2} and dot height of 24.3nm, respectively for uncapped InN. By increasing the capping temperature the dots were deformed and the dot density decreased. The similar trend was also observed in photoluminescence (PL) spectra. The InN band to band emission appeared clearly around 0.77eV that agreed with recent reports. Besides that is consistent, the PL intensity of InN emission decreased with the increasing capping temperature with AFM

observations. Moreover, another two strong visible emission bands at 2.975eV (violet emission) and 2.37eV (green emission) were observed. From the analysis of high angle X-ray diffraction curves of capped samples, we found two peaks at 71.7° and 70.2° that may be due to InGaN formation. It is likely that the visible emissions are from InGaN formed by capping processes, though other causes such as deep levels defects cannot be excluded completely. We further analyzed the spatial distribution of PL signals by NSOM mapping and suggest that the visible emissions come from both the capping and interface layers.

Chapter 1 Introduction

Developments in the III-nitride (InN, GaN, and AlN) semiconductors have been spectacular due to their attractive inherent properties. During the last few years, the interest in the InN has been remarkable. The number of publications concerning InN research has increased significantly in recent years. Indium nitride (InN) is an important III-nitride semiconductor with many potential applications. The use of InN and its alloys with GaN and AlN makes it possible to extend the emission of nitride-based LEDs from the ultraviolet to infrared region [1,2]. In addition, InN is a potential material for low cost solar cells with high efficiency. *Yamamoto et al.* proposed InN for a top cell material of a two-junction tandem solar cell [3].

The combination of the inherent properties of InN and self-assemble nanostructures with quantum confinement effects presents further potential uses for this material. Moreover, quantum dot (QD) structures are especially promising because they act as electron-hole recombination centers. However, high-quality InN deposition is still not well established due to the complexity required for good epitaxial growth. The growth of InN is the most difficult among the III-nitrides because of the low InN dissociation temperature and high equilibrium N_2 vapor pressure over the InN. The InN requires a low growth temperature that is between 400℃ and 700℃ [4]. However, the most suitable growth temperature of GaN is around 1050℃. The suitable growth temperature for InN and GaN is conflicting to each other. In order to achieve better quantum

confinement effect, we must have better quality of GaN capping layer by increasing the capping temperature. However, InN is easily deformed and dissociated at high temperature. Thus, we need to find a compromised growth temperature to keep the InN quality and to hold the confinement effect. Therefore, the capping temperature is one of the important factors in InN growth process. In this thesis, we will study the capping effect on InN samples prepared by metal organic chemical vapor deposition (MOCVD) system.

Chapter 2 Theoretical backgrounds

2.1 Wurtzite structure

The crystal structures for group-III nitrides include wurtzite and zinc-blende as shown in Fig. 2-1-1, in which wurtzite structure is more stable at ambient condition. Wurtzite structure consists of two hexagonal close packed sub-lattices, each with one type of atoms, and the two are offset along the c axis by 5/8 of the cell height. The stacking sequence of (0001) planes is ABABAB in the <0001> direction and each group-III atom is coordinated with four group-V atoms. Our samples are wurtzite InN.

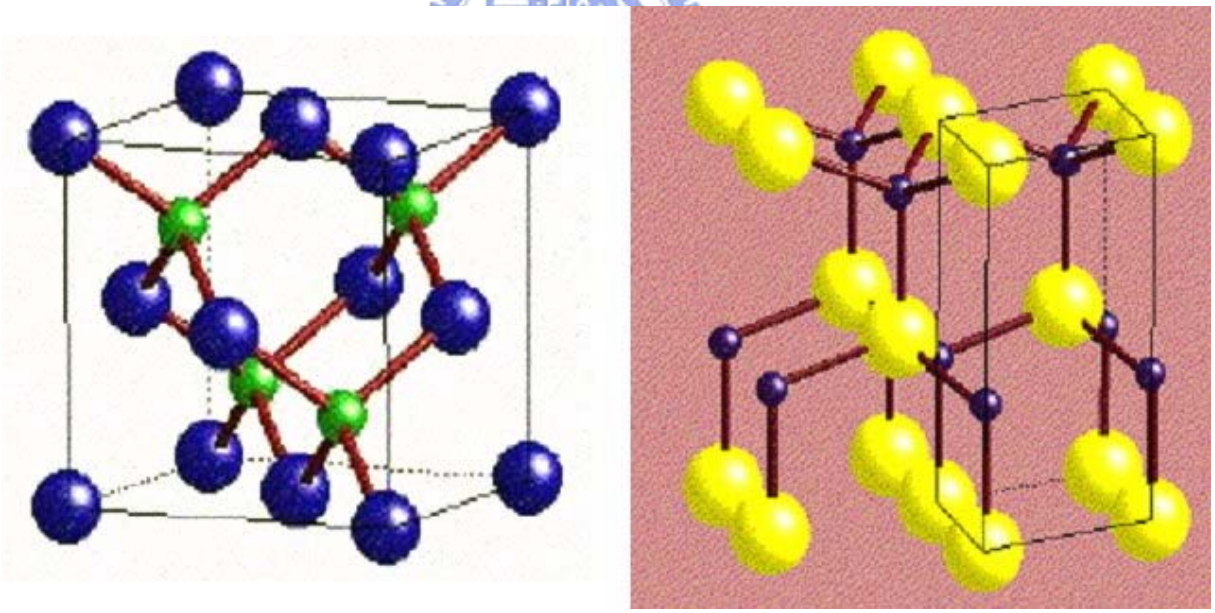

(a) (b)

Fig. 2-1-1 Schematic diagram of (a) Zinc-Blende structure and (b) Wurtzite structure.

2.2 Photoluminescence in Semiconductors

As the laser beam irradiates a semiconductor, electrons and holes can be created if the photon energy is larger than the semiconductor band gap. The electrons and holes may be scattered and then redistribute near the conduction band minimum and the valence band maximum, through the process of carrier-phonon interaction. Under the quasi-thermal equilibrium, electrons and holes may recombine and produce photons. If the defects or impurities exist in the semiconductors, the electron-hole pairs may recombine and create photons via the levels formed by defects and impurities, these levels are often called "radiative centers". Furthermore, defects and impurities may also create "non-radiative centers", at which the electron-hole pairs are absorbed but do not emit photons, so that the emission efficiency will be reduced. Two types of recombination are described as follows:

(A) Radiative Transition

(I) Band to Band Transition

In perfect semiconductors, the excited electrons and holes will accumulate at the conduction band minimum and valence band maximum. As shown in Fig. 2-2-1, electron-hole (e-h) pairs will recombine radiatively with high probability (in the direct band gap semiconductor). The recombination rate is proportional to the electron (n)–hole (p) concentration. The recombination rate can be expressed as :

$$R = \int R(h\nu)d(h\nu) \sim np$$

But in the indirect band gap semiconductors, the transition must involve an additional particle – "phonon" (in order to satisfy the momentum conservation law). Thus, the transition probability will be reduced, and the emission efficiency is lower than that of the direct band gap semiconductors. Most of Ⅲ-Nitrides (such as InN、GaN、AlN) are the direct band gap semiconductors.

(II) Exciton Transition

In high quality semiconductors, the Coulomb interaction between the conduction band electrons and the valence band holes will result in the formation of the bound electron-hole pairs, that is the so called "exciton". The exciton is analogous to "positronium atom" – an electron bound to a positron, and this quasi-particle (exciton) is electrically neutral. In most Ⅱ-Ⅳ、Ⅲ-Ⅴ semiconductors, the exciton radius (Bohr radius) is large in comparison with the lattice length of the unit cell, they are called "Wannier excitons". Beside this, if the radius of the excitons is on the order of or smaller than an atomic unit cell, these are called "Frenkel excitons".

(III) Donor Acceptor Pair Recombination (DAP)

The impurities present in the semiconductors may form the donor (positive) or the acceptor (negative) levels in the energy gap. The electrons and holes created by the laser excitation may be bound to the donor (D^+) and the acceptor (A^-) to form the neutral donor (D^0) and acceptor (A^0). If the neutral donor electron and the acceptor hole recombine, as expressed by:

$$D^0 + A^0 \rightarrow h\nu + D^+ + A^-$$

It can emit photon with energy:

$$E_{DAP} = h\nu = E_g - (E_D + E_A) + \frac{e^2}{\varepsilon \cdot R_{DA}}$$

Where, E_g is the energy gap of semiconductor, E_D and E_A is the binding energy for the electron to the donor and the hole to the acceptor respective. R_{DA} is the distance between the donor and the acceptor. If the R_{DA} increases, the transition probability will reduce, so does the PL intensity.

(B) Non-Radiative Transition

There are several transitions that compete with the radiative transition and thus reduce the emission efficiency. They are described as follows:

(I) The e-h pair is scattered by the phonon or carriers and loses its energy.

(II) The e-h pair recombines at defect, dislocation, grain boundary or surface, and loses its excess energy, the so-called "cascade process".

(III) The e-h pair loses its energy via the "Auger process" that involves the core level transitions.

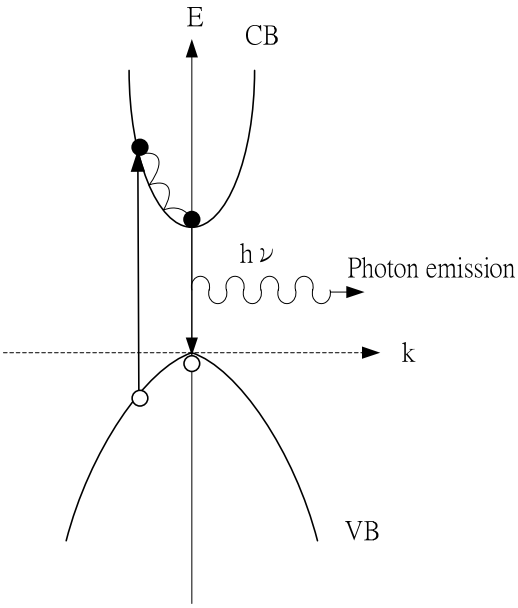

(a) Direct transition

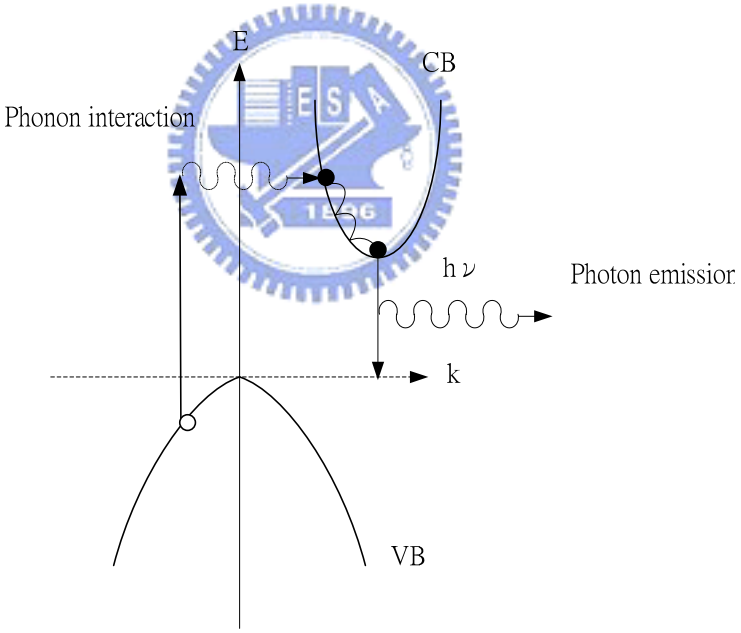

(b) Indirect transition

Fig. 2-2-1 The schematic diagram of (a) direct transition and (b) indirect transition.

Chapter 3 Experiments

In this chapter, we describe the sample preparation of flow-rate -interruption epitaxy (FME) method grown InN nano-dots and the configuration of experimental systems.

3.1 Sample preparations

The samples investigated were grown on sapphire (001) by MOCVD using trimethylgallium (TMGa), trimethylindium (TMIn) and NH_3 as source materials with GaN buffer layer grown at 1050℃. The InN nano-dots were then grown at 700℃ by using flow-rate -interruption epitaxy (FME) method. The gas flow sequence for FME, if not mention elsewhere, basically consists of four steps: 20-sec TMIn source step, 20-sec NH_3 source step and the intervened 10-sec purge steps in between. It is worth to mention that during 20-sec TMIn source and 10-sec purge steps a small amount of NH_3 (4.46×10^5 μmole/min) is also introduced intentionally in order to suppress the re-evaporation of adsorbed nitrogen atoms. After the growth of InN dots, the substrate temperature was then decreased under a continuous flush of NH_3 gas for the growth of a 35 nm-thick GaN cap layer. The series of samples changed the capping temperature from 600℃ to 730℃. Fig. 3-1-1 showed the schematic diagram of the series of samples. The growth condition of each sample was listed in Table 3-1-1.

Sample	*a*	*b*	*c*	*d*	*e*	*f*
Growth temperature	700℃	700℃	700℃	700℃	700℃	700℃
Capping temperature	uncapped	600℃	675℃	700℃	715℃	730℃

Table 3-1-1 The growth condition of InN nano-dots.

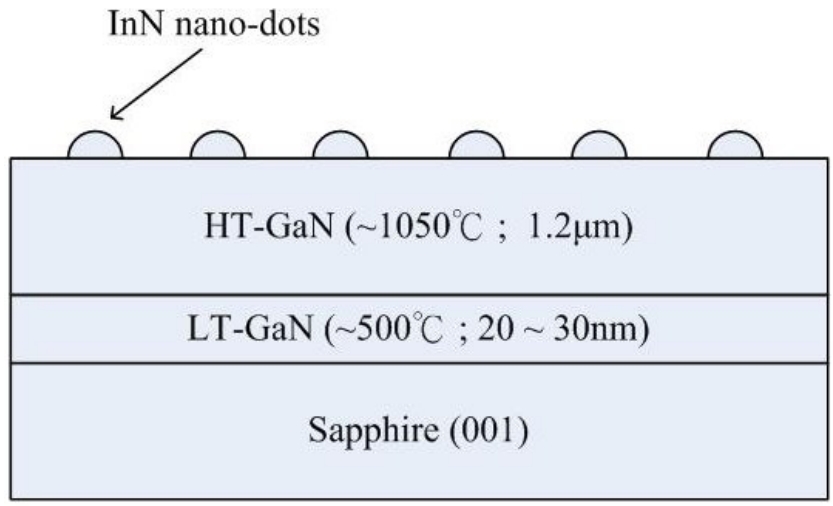

(a)

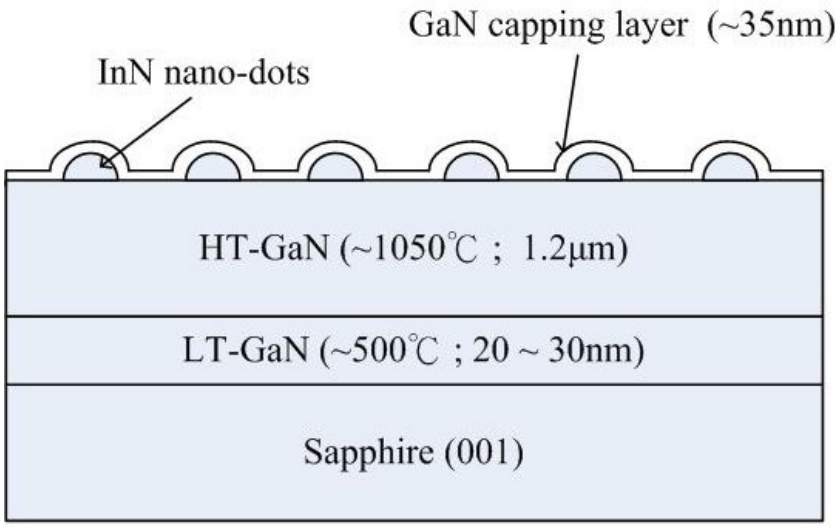

(b)

Fig. 3-1-1 Schematic diagram of (a) sample *a* (uncapped) and (b) sample *b-f* (capped).

3.2 Atomic force microscopy (AFM)

Gerd Binning and Calvin F. Quate invented atomic force microscopy (AFM) in 1986 [6]. They realized that it is able to measure interactive force between atoms of the tip and sample surface by using special probe which consists of a flexible, elastic cantilever and sharp probe tip.

Fig. 3-2-1 shows the configuration of AFM. The sharp tip locates at the free end of a flexible cantilever attached to the scanner. The scanner controls two independent movements of the cantilever: scanning along the sample surface (X-Y plane) and movement perpendicular to the surface (along the Z-axis). The scanner is made of the piezoelectric material that expands or shrinks depending on the applied electrical voltage. When the cantilever is bent by the repulsive or attractive force from the interaction between the tip and the surface atoms of sample, it causes the change of the deflection. During scanning, the detection system measures the cantilever deflection from its initial position and then sends a signal proportional to the deflection value to the scanner control system. The feedback signal is used to move the probe up or down by the piezo-electric crystal to bring the parameter back to its original values. Simultaneously, the probe displacement value is recorded by computer and interpreted as the specimen topography.

AFM can be operated in contact, non-contact, or tapping mode. In contact mode, the tip touches the surface and scans over the sample. Although high resolution can be obtained in this way, the deformation of tips or samples often

happens. Non-contact mode is preferred to avoid the probe deformation since it utilizes the long range Van der Waal's force between the tip and specimen. However, the sensibility and resolution is limited because of the interference from ambient environment. Tapping mode is a combination of contact mode and non-contact mode. Detection of tapping mode is more sensitive than that in non-contact mode and less destructive on probes or specimen than that in contact monde.

Scanning probe microscopy (SPM) system used in our study is Slover P47H, manufactured by the "Molecular Devices and Tools for Nano Techology (NT-MDT)" in Russia. It can be operated in multi-modes such as AFM for morphology measurements, EFM, MFM, and SKM, etc. In our studies, the InN nano-dots' morphology was measured by tapping mode in order to optimize the resolution and avoid probe destruction. The AFM probe, which has a cantilever about 50 or 80 μm and a sharp tip with a radius of curvature about 10 nm (Fig. 3-2-2), is also from NT-MDT.

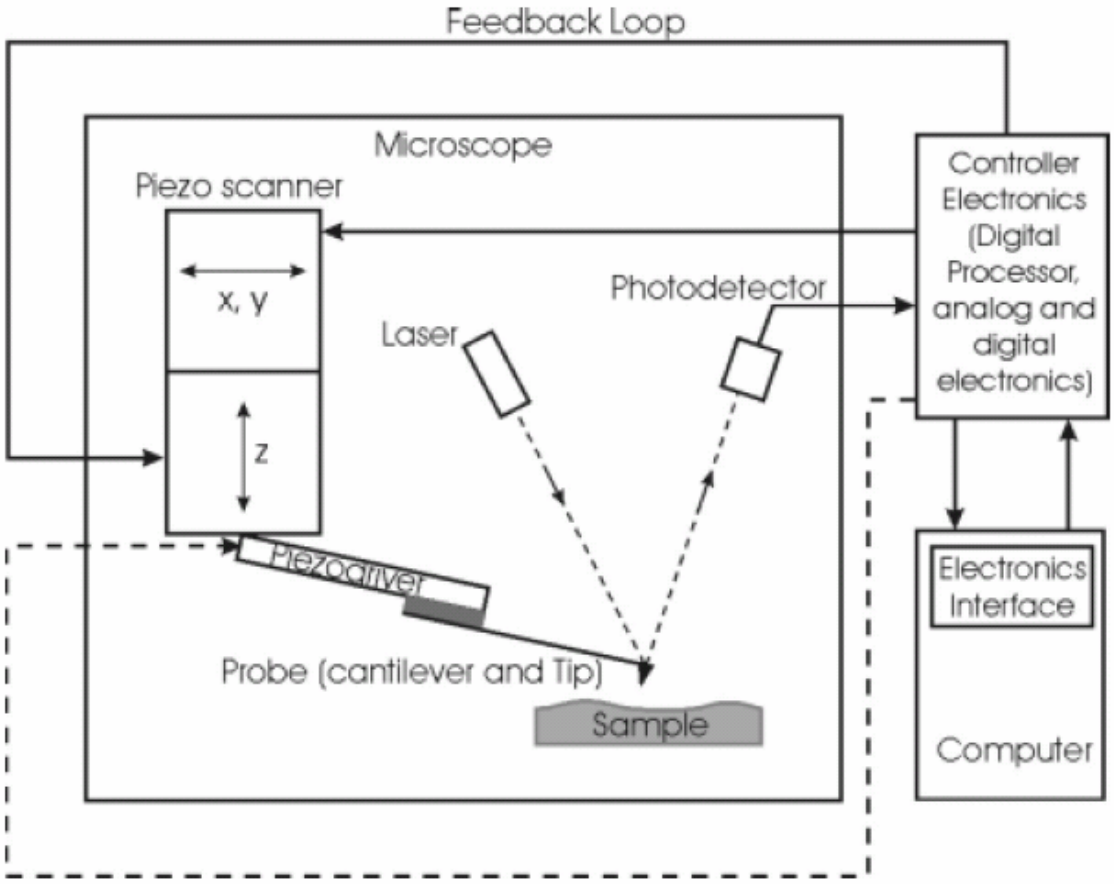

Fig. 3-2-1 Schematic diagram of AFM system.

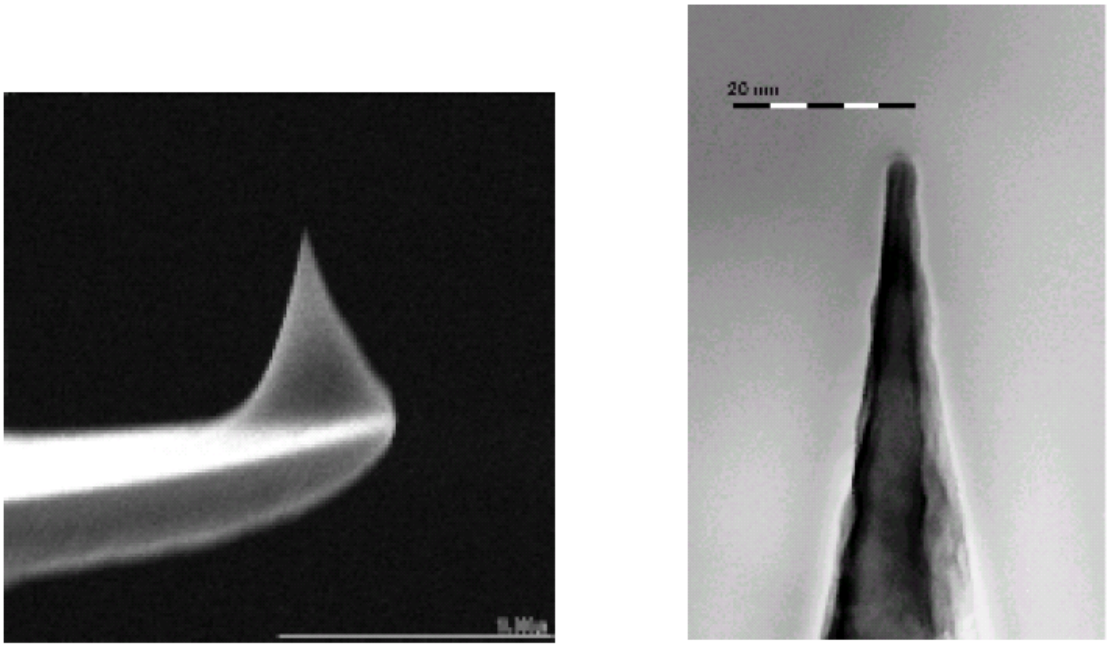

Fig. 3-2-2 The SEM image of scanning probe and the tip.

3.3 Micro-photoluminescence (μ-PL) system

Micro-photoluminescence (μ-PL) system incorporated the Olympus BH2 optical microscope is shown schematically in Fig. 3-3. A He-Cd laser (Kimmon) is used as the excitation light source. The optical paths for visible region and infrared signals can be switched conveniently in this system.

I. **The visible signals:**

Laser operating at the 325nm UV line was used as the excitation light source and the output power is 25mW. The beam is reflected by UV mirrors and then incident into the microscope, passing through a 50%-50% beam splitter and focused by a long-working distance near-UV objective lens (Mitutoyo NUV 100X, N.A. = 0.5). The laser beam was focused on the sample, with a spot size $\leqq$ 3μm. The luminescence signals from samples were collected by the same objective lens, then reflected by the beam splitter and coupled into the optical fiber. The signals were then transported through optical fiber then and the 325nm long-pass edge filters (for blocking laser intensity) and coupled into the monochrometor. Finally, the signals were dispersed by ARC Pro 500 monochrometor (whose spectrum resolution is about 0.2nm with both the entrance and exit slits opened to 50μm), detected by the Hamamatsu R943-02 photomultiplier tube, and processed using lock-in amplifier (Stanford SR530) and Acton Spectra Hub.

II. **The infrared signals:**

For infrared signals, laser operation at 442nm lines was used as the

excitation light source with output power ~ 95mW. The beam passed through a 442nm band-pass filter to ensure that the excitation source is pure from 400nm to 2000nm. The laser beam was focused by a long-working distance near-IR objective lens (Mitutoyo NIR 50X, N.A. = 0.42) on sample, with a spot size ≦ 5μm. The luminescence signals were collected by the same objective lens, reflected by the beam splitter, blocked laser intensity by 850nm color filter (Thorlabs), and coupled into the monochrometor (ARC Pro 500). The dispersed signals were detected by the EOS extend InGaAs detector, and processed using lock-in amplifier (Stanford SR530) and Acton Spectra Hub.

Low-temperature micro-PL was carried out using a closed cycle cryogenic system (APD HC-2D). The temperature was varied from 10K to 300K by Lakeshore 330 temperature controller.

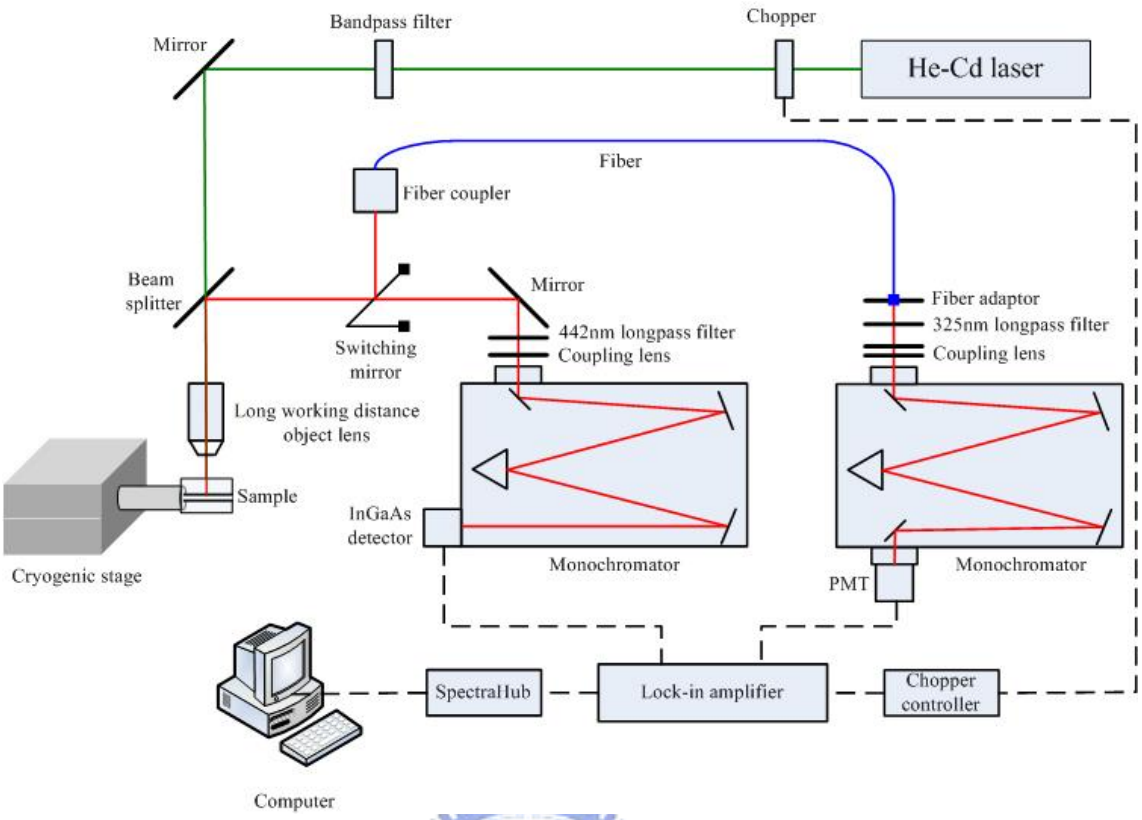

Fig. 3-3 Schematic diagram of micro-PL system.

3.4 Near-field scanning optical microscopy (NSOM) system

NSOM includes two important parts: the optical coupling system and the NSOM scanning probe. We describe them separately in the section.

I. Experimental setup

Fig. 3-4-1 showed the schematic diagram of NSOM system. The scanning measurement was performed with Solver SNOM (Olympus based) developed by NT-MDT. A He-Cd laser (Kimmon) operated at the 325nm is used as the excitation light source. Laser is reflected from the edge filter (Semrock, LP02-364RU), coupled to the multimode fiber and illuminated on the sample through probe made by chemical etching. The PL signals were collected by the same probe and passed through the edge filter that blocked the excitation laser intensity. The PL signals were dispersed by ARC Pro 500 monochrometor and detected by the Hamamatsu R955 photomultiplier tube. The PMT signals were processed by lock-in amplifier (Stanford SR530) and the Solver SNOM controller. The system treated the PL signals and topography images at the same time to show the NSOM mapping image.

II. Fabrication of NSOM probe

The optical probe is the most critical part of the near-field microscope for achieving high resolution images. NSOM probes have been fabricated from a variety of materials, including cleaved crystals, atomic force microscope (AFM) cantilever tips, semiconductor structures, glass pipettes, and tapered optical fibers [7]. Following fabrication of the tapered tip, the sides of the probe are

coated with an opaque metal film (usually aurum, platinum, or aluminum) to prevent light loss in regions of the waveguide other than the aperture. There are many different ways to fabricate and characterize near-field optical probes. There are a variety of techniques that have proven useful for fiber tapering, but the task is most commonly accomplished by chemical etching or by heating and pulling, and in some cases both methods are combined to achieve the desired taper characteristics. Our NSOM probe was made by chemical etching of BOE solution ($HF:NH_4F$ = 1:6) and coated with platinum metal film by using ion sputter (Hitachi E-1010). Then, the probe was adhered to a tuning fork with the resonance frequency at 32.768KHz. Fig. 3-4-2 showed the SEM image of coated tip.

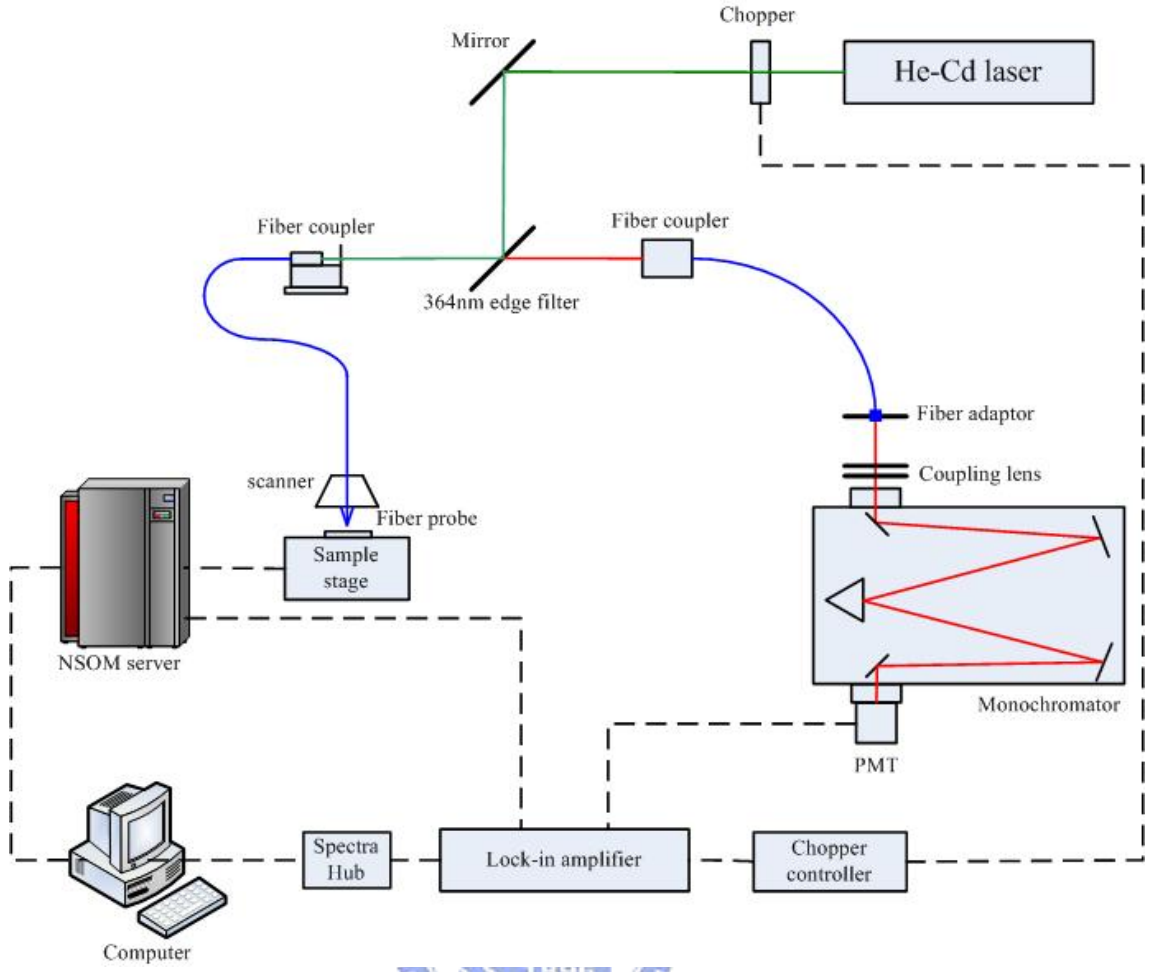

Fig. 3-4-1 Schematic diagram of NSOM system.

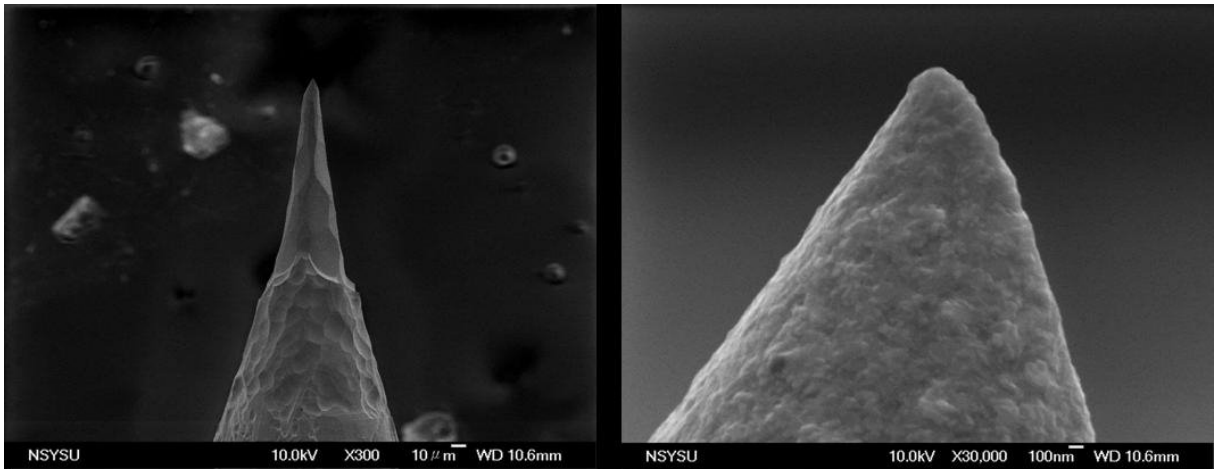

Fig. 3-4-2 The SEM image of coated tip.

Chapter 4 Results and discussion

In this chapter, we first discuss the morphology of InN nano-dots by AFM imaging and then the optical characteristics by micro-PL measurements. We also examined X-ray diffraction curves of emissions what to show are concurred in PL spectra. Furthermore, NSOM mapping provided the spatial correlation between AFM morphology and PL features. From these results, we will propose a model to explain the visible emission bands in PL spectra.

4.1 Surface morphology of InN nano-dots

AFM morphology images of InN nano-dots grown on GaN buffer layer are shown in Fig. 4-1-1. Image (a) showed the 2μm×2μm plane view of uncapped sample *a* with dot density of 3.9×10^{8} cm^{-2} and average dot height of 24.3nm. In this image, we can see that the surface of GaN buffer layer is very flat and the profile of InN nano-dots is hexagonal. It showed that the InN nano-dots are successfully grown.

Samples *b* to *f* are capped with GaN at different temperature whose morphology are shown in Figs. 4-1-1 (b) to (f). The average dot density and dot height taken from 10μm×10μm image are shown in Table 4-1-1.

We can see that the dot profile of sample *b* is very similar to that of sample *a*. Their dot densities are approximate the same. However, the dot height of sample *b* is shorter than that of sample *a* as due to the capping effect. When the capping temperature is raised to 675℃, InN nano-dots appear to be deformed with irregular profiles and some are merged. The average dot height decreases even

further when the capping temperature reaches 700℃, 715℃ and 730℃. For these cases, both the dot deformation and merge are more evident as shown in Fig. 4-1-2. The phenomenon reveals that InN becomes unstable at high temperatures. It might be due to indium diffusion or nitrogen outgasing that made dot profile deform and dot density decrease. Furthermore, the sample surface is no longer flat roughened forming GaN capping layer. The most suitable growth temperature is around 1050℃ for GaN that displays smooth and flat surface as shown in Fig. 4-1-1 (a). However, for the capping temperature of GaN between 600℃ and 730℃, its growth rate is in kinetic mode that may cause a rough surface.

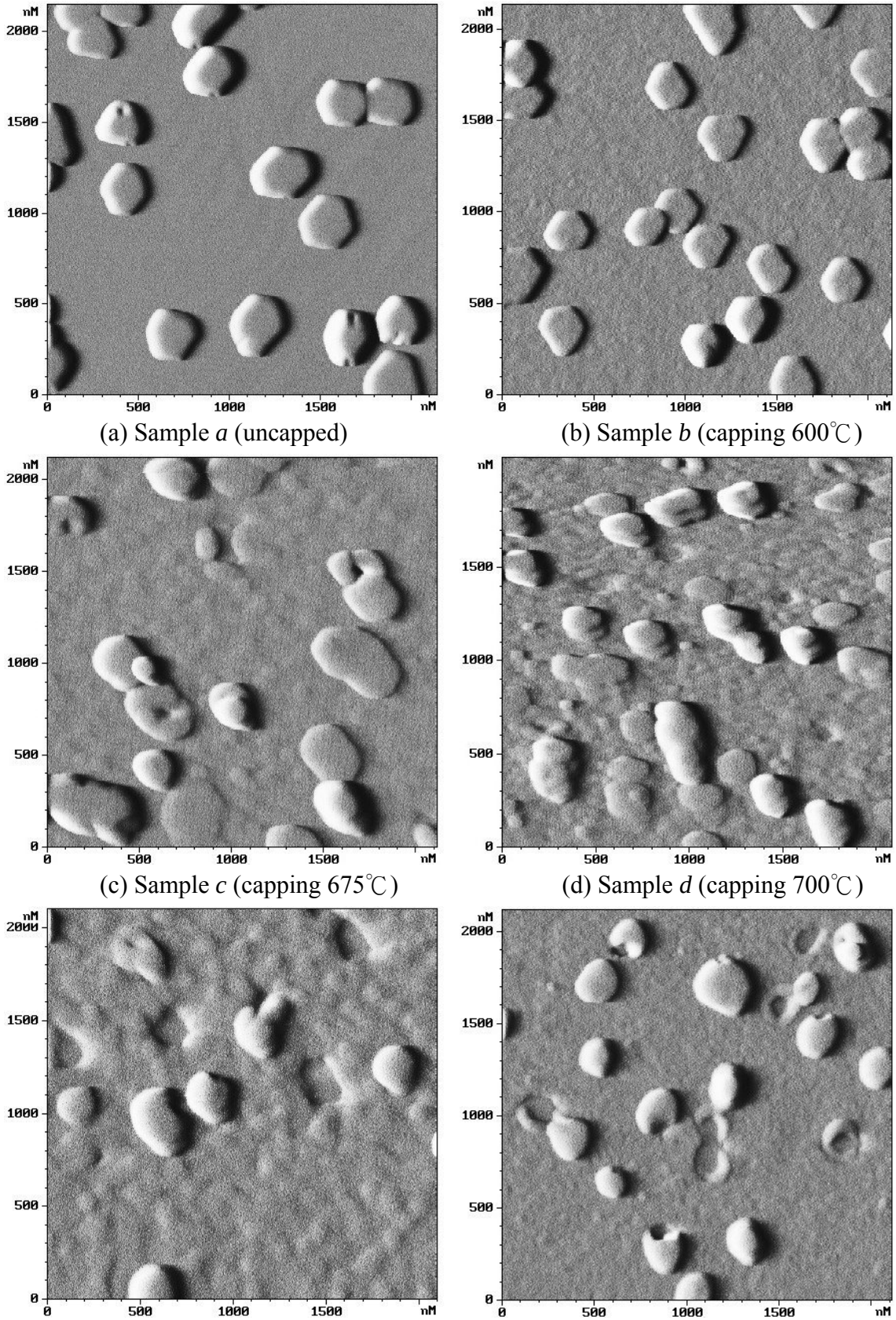

(a) Sample *a* (uncapped)

(b) Sample *b* (capping 600℃)

(c) Sample *c* (capping 675℃)

(d) Sample *d* (capping 700℃)

(e) Sample *e* (capping 715℃)

(f) Sample *f* (capping 730℃)

Fig. 4-1-1 AFM morphology images of InN nano-dots.

Sample	*a*	*b*	*c*	*d*	*e*	*f*
Capping temperature	uncapped	600℃	675℃	700℃	715℃	730℃
Dot density (cm^{-2})	3.9×10^{8}	3.8×10^{8}	3.5×10^{8}	3.6×10^{8}	2.4×10^{8}	2.5×10^{8}
Dot height (nm)	24.3	19.8	18.3	15.1	13.5	13.7

Table 4-1-1 Average dot density and height of InN nano-dots taken from 10μm×10μm image.

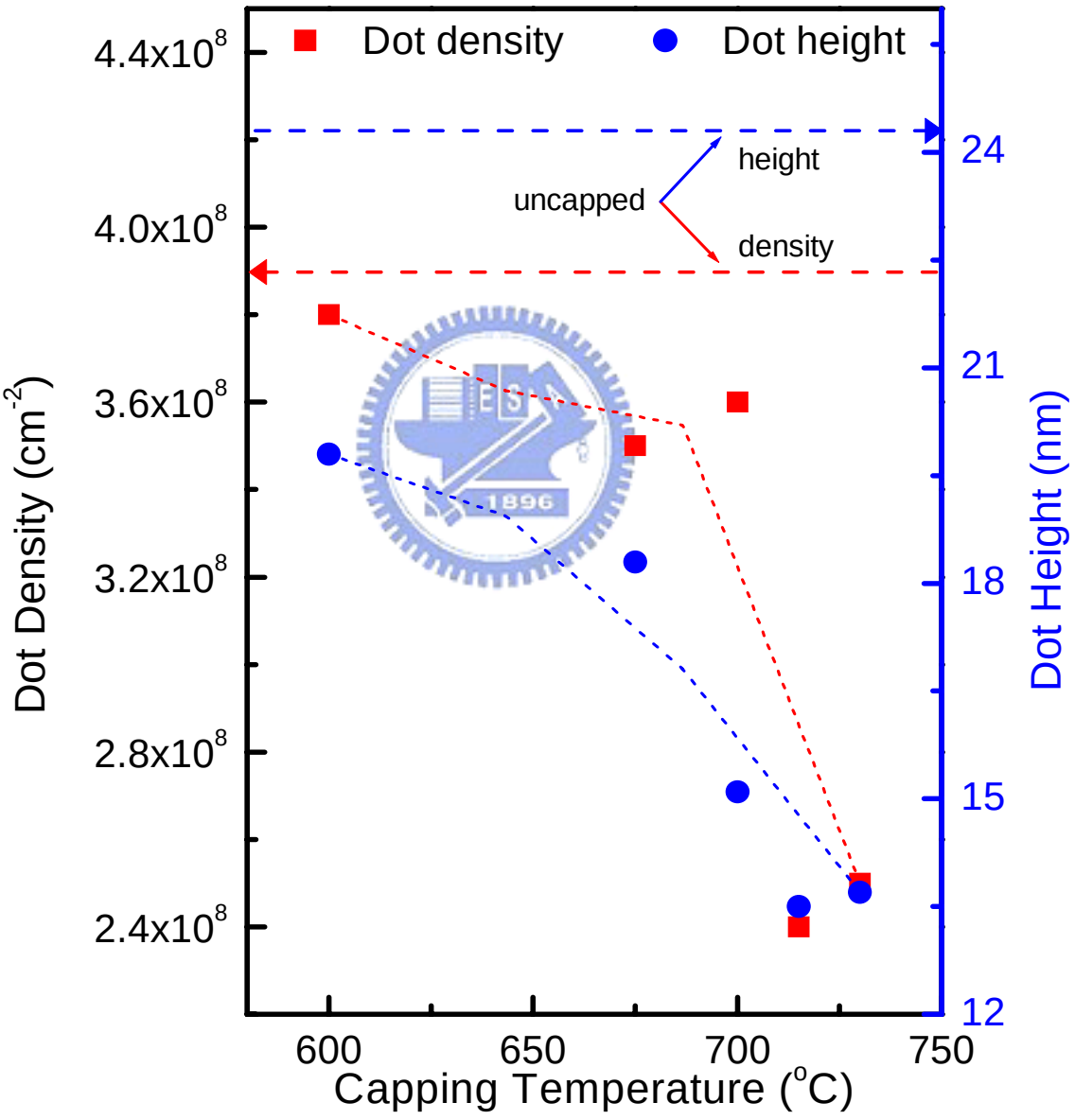

Fig. 4-1-2 The average dot density and dot height variation.

4.2 Micro-PL spectra of InN nano-dots

The PL spectra at 10K of InN nano-dots are shown in Fig. 4-2-1. Fig. 4-2-1 (a) to (f), respectively, for both uncapped and capped with GaN at 600, 675, 700, 715, and 730℃. The peak of 3.48eV is ascribed to the near band edge emission (NBE) of GaN [8]. The peak about 0.77eV is due to InN nano-dots. Recently InN PL and absorption measurements suggested that the bandgap energy of this material is around 0.7eV [5,9,10] rather than about 2eV [11] as had been previously accepted . Our PL data agreed with references. When InN nano-dots were uncapped, the position of InN band to band transition peak was 0.77eV and its intensity was the strongest. The InN band transition is the main radiation transitions and no other emission peaks except the NBE of GaN. By increasing the capping temperature from 600℃ to 730℃, the peak intensity decreased clearly. Obviously, the capping effect degrades the InN emission by competitive emission channels. Fig. 4-2-2 showed the integrated intensity variation with increasing capping temperatures of InN band transition peaks at 10K. This conclusion conforms to the result of AFM images. So, the InN band transition intensity decreased may be due to the degraded quality of InN nano-dots. The dot density decreased clearly and quality became worse at 715℃ and 730℃ capped temperature. It made the FWHM became broader. Fig. 4-2-3 showed the peak position and FWHM of InN band transition at 10K.

We observed that as the capping temperature exceeded 600℃, other peaks appeared except the infrared peak. The strong violet emission around 2.975eV

appeared when the capping temperature was above 675℃, and its intensity was the strongest at 700℃. By further increasing the capping temperature, another green emission appeared around 2.370eV. When the 2.370eV peak became large, the 2.975eV peak became weak. They are shown in Fig. 4-2-4. It is evident that the visible PL peaks are from two competitive radiative transitions. When 2.370eV emission appeared, it became the main radiative transitions and 2.975eV emission decreased.

In the beginning of this thesis work, we did not expect the visible emissions from InN nano-dots. In fact, the visible emissions are so obvious in our samples after capping. Its origination may be either from deep levels in GaN with various defects [12-14] or due to InGaN formation at high capping temperature according to references [23]. In next section, we focused our studies on the origination of the 2.370eV and 2.975eV peaks, by analyzing X-ray diffraction curves and NSOM mapping spectra to discuss in depth the origination of these visible emission peaks.

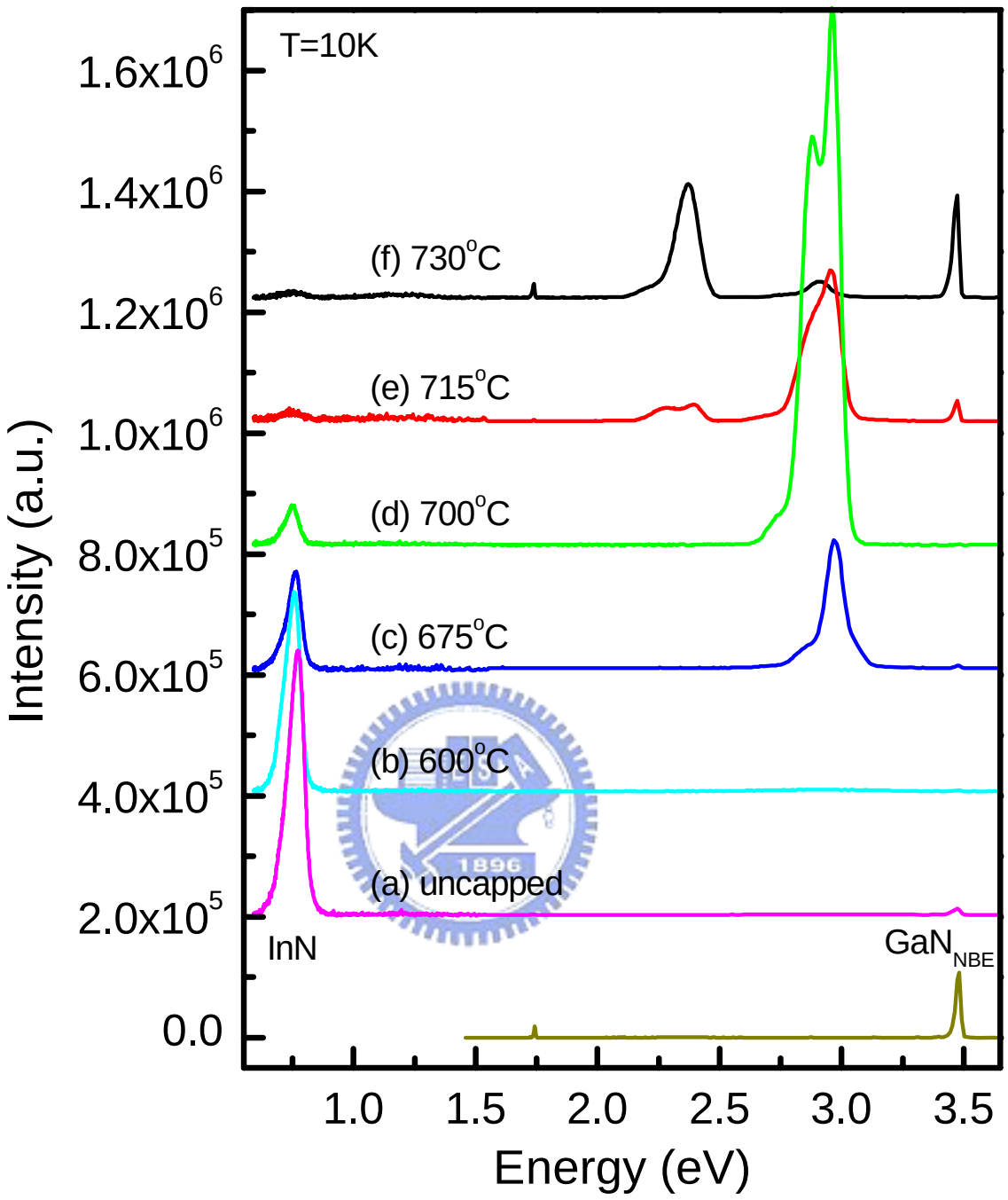

Fig. 4-2-1 PL spectra of 700℃ grown InN nano-dots on GaN film, (a) without capping, and with different capping temperatures, (b) 600℃, (c) 675℃, (d) 700℃, (e) 715℃, and (f) 730℃ from UV to IR regions.

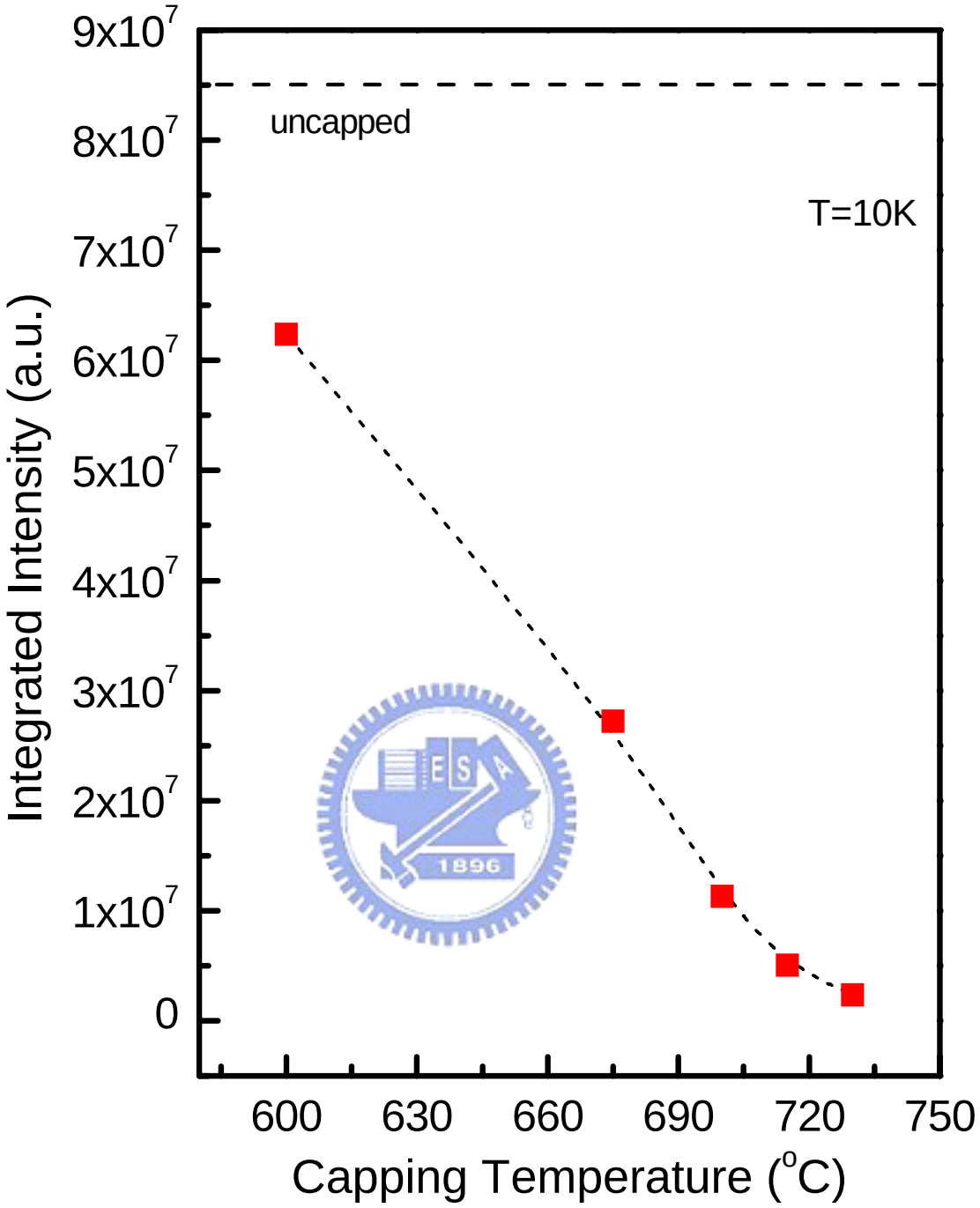

Fig. 4-2-2 The integrated intensity of InN peak decreased with the increasing capping temperature.

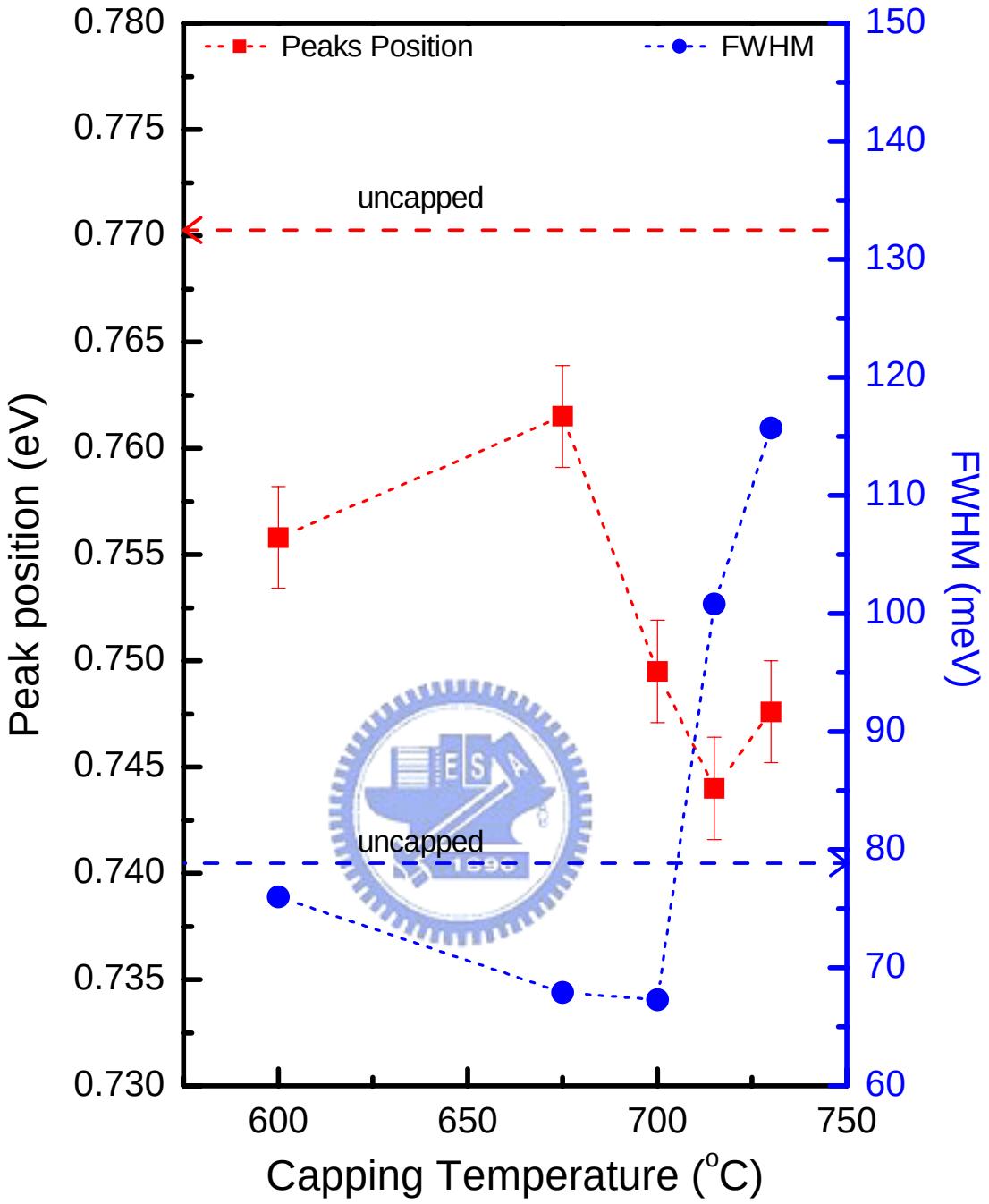

Fig. 4-2-3 The variation of peak position and FWHM of InN band transition vs. capping temperature.

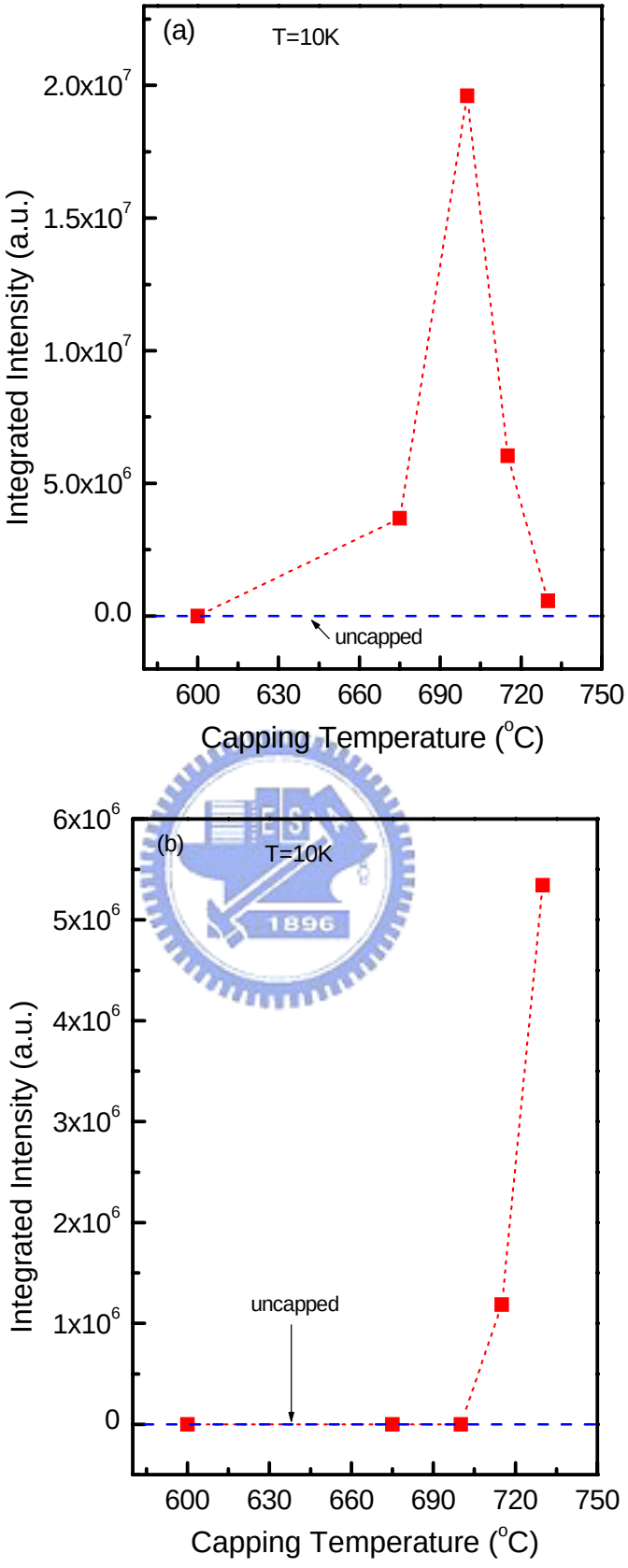

Fig. 4-2-4 The integrated intensity of (a) the violet (2.975eV) and (b) the green (2.370eV) emission bands.

4.3 X-ray diffraction curves of InN nano-dots

In this section, we further studied the origination of these visible PL peaks by analyzing X-ray diffraction curves. The compositional variation and quality of InN nano-dots under different capping temperatures were examined. We found the correlation between the visible PL peaks and the compositional variation of InGaN or GaN related defects. Because defect states can not form crystalline structure, there should be no corresponding X-ray diffraction signals.

Fig. 4-3-1 showed the X-ray diffraction curves obtained for this series of samples. In curve (a), we saw only that 2θ angles of InN and GaN (0002) crystal face are 31.14° [15-17] and 34.42° [18-20] respectively. Thus, we believed that InN nano-dots without capping layer have aligned crystal axis along GaN (0002) direction.

Fig. 4-3-1 (b) to (f) showed X-ray diffraction curves of sample *b* to *f* respectively. It is obvious that a distinct feature at 33.1° on the shoulder of GaN when the capping temperature increased. This may come from InN $(10\bar{1}1)$ [15-17,21] or compositional InGaN phase. In order to analyze this feature in detail, we did high angle X-ray diffraction hoping that separation between InN (0004) and GaN (0004) may reveal more details about the shoulder.

As shown in Fig. 4-3-2, the angles of InN and GaN (0004) phases are 65.13° [15-17,21] and 72.84° [18-20] respectively. Because the GaN intensity is too strong, we only show the data range between 64° and 72°. It is evident that new peak appears around 70°. This should be associated with the feature around 33°

in low angle X-ray diffraction. After subtracting GaN background from these high angle X-ray diffraction curves, it reveals much detailed feature in Fig.4-3-3.

By proper fitting, all peaks from Fig. 4-3-3 (f) were labeled in top. In curves (d), (e), and (f), the peak position around 69.4° is close to the InN ($20\bar{2}2$) peak mentioned in references [21,22]. The appearance of InN ($20\bar{2}2$) peak is for the capping temperature of 700℃ and above. As AFM images showed in section 4-1, the density of InN nano-dots decreased rapidly with facet that may contain ($10\bar{1}1$), ($20\bar{2}2$) phase. By the capping temperatures increasing, this peak intensity rises and falls and peaked at 715℃.

There are also two other peaks around 71.7° in curves (b) to (f) and around 70.2° in curves (e) and (f). They correspond to the shoulder which we are interested in the low angle X-ray diffraction. Since the point defects or native defects of GaN usually mentioned in references have no characteristic peaks in X-ray diffraction. We tend to believe that they are due to InGaN formation.

By linear interpolation, the corresponding $In_xGa_{1-x}N$ compositions of 71.7° and 70.2° peaks are 14.79% and 34.24% respectively. Using Vegard's law, we can calculate the bandgap energy:

$$E_g = x \cdot E_g(InN) + (1-x) \cdot E_g(GaN) - b \cdot x \cdot (1-x)$$

Considering the bowing parameter, b = 0.9, the bandgap energies of 14.79% and 34.24% InGaN are 2.96eV and 2.35eV, respectively. These two energies

just falls on two visible emission peaks in PL spectra as discussed in section 4-2.

Fig. 4-3-4 showed the integrated intensity of (a) InN(0004) 65.13° (b) 71.7° and 70.2° peaks. By comparing Fig. 4-2-2 with Fig. 4-3-4 (a), we see that the peak around 65.13° in X-ray diffraction curves has the same felling trend as the peak around 0.77eV in PL spectra. The similar situation appears in Fig. 4-2-4 (b) and Fig. 4-3-4 (b), that the peak around 70.2° in X-ray diffraction curves has the same rising trend above 700℃ as the peak around 2.37eV in PL spectra. As for the 71.7° peak and 2.975eV peak, they showed more complex behavior. The PL intensity is affected by the band structure as there may be several competitive radiation transitions. The peak around 2.975eV has the strongest emission at 700℃, since the InN band emission is dominant at 600℃ and 675℃, while 2.37eV green emission becomes the main transition at 715℃ and 730℃. Peak around 71.7° in Fig. 4-3-4 has also drastic variation between 675℃ and 730℃.

Based on X-ray diffraction results, the violet and green emission peaks in PL spectra are closely related to InGaN formation.

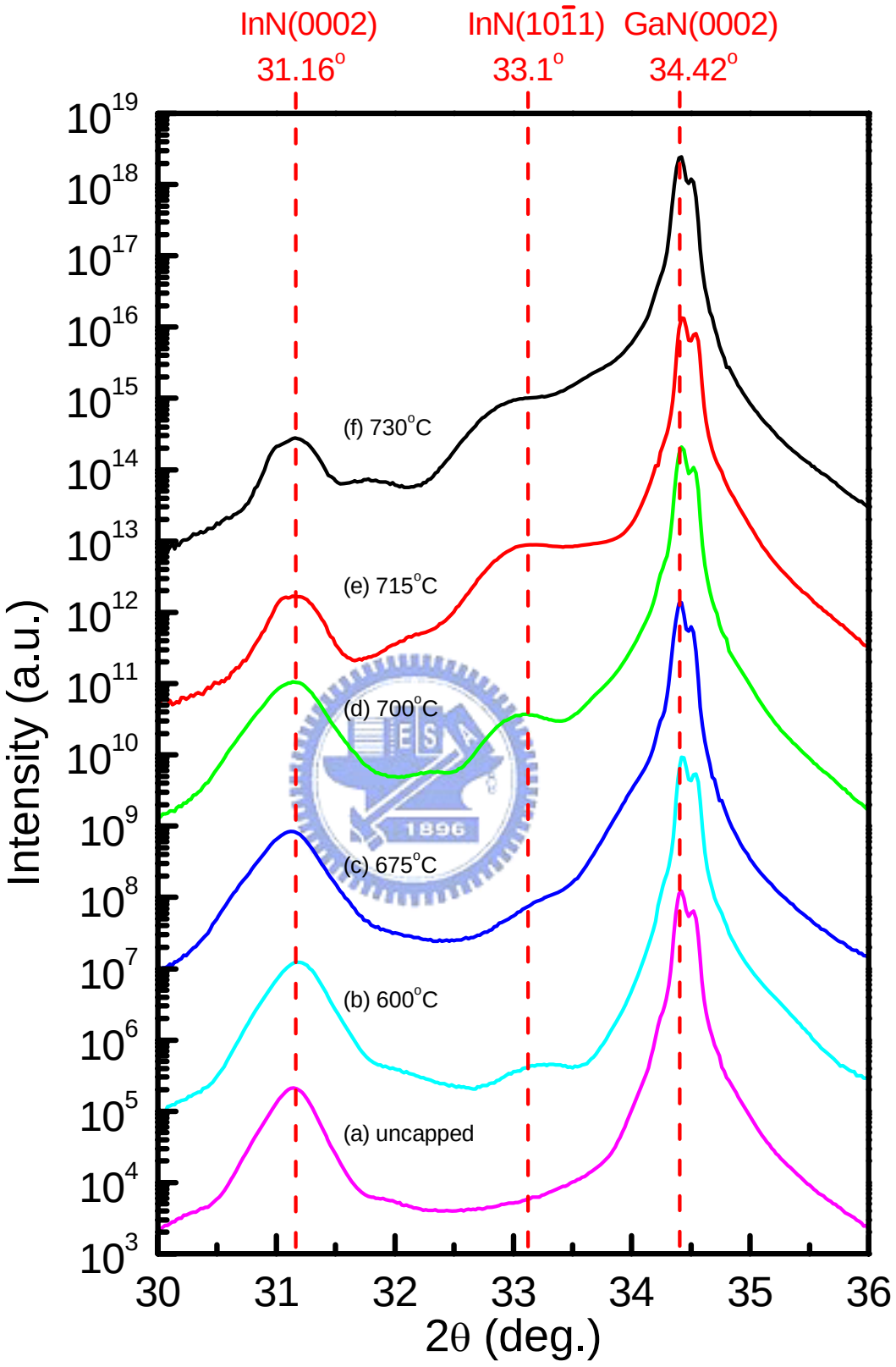

Fig. 4-3-1 X-ray diffraction curves of 700℃ grown InN nano-dots on GaN film without capping, (a), and with different capping temperatures, (b) 600℃, (c) 675℃, (d)700℃, (e) 715℃, and (f)730℃.

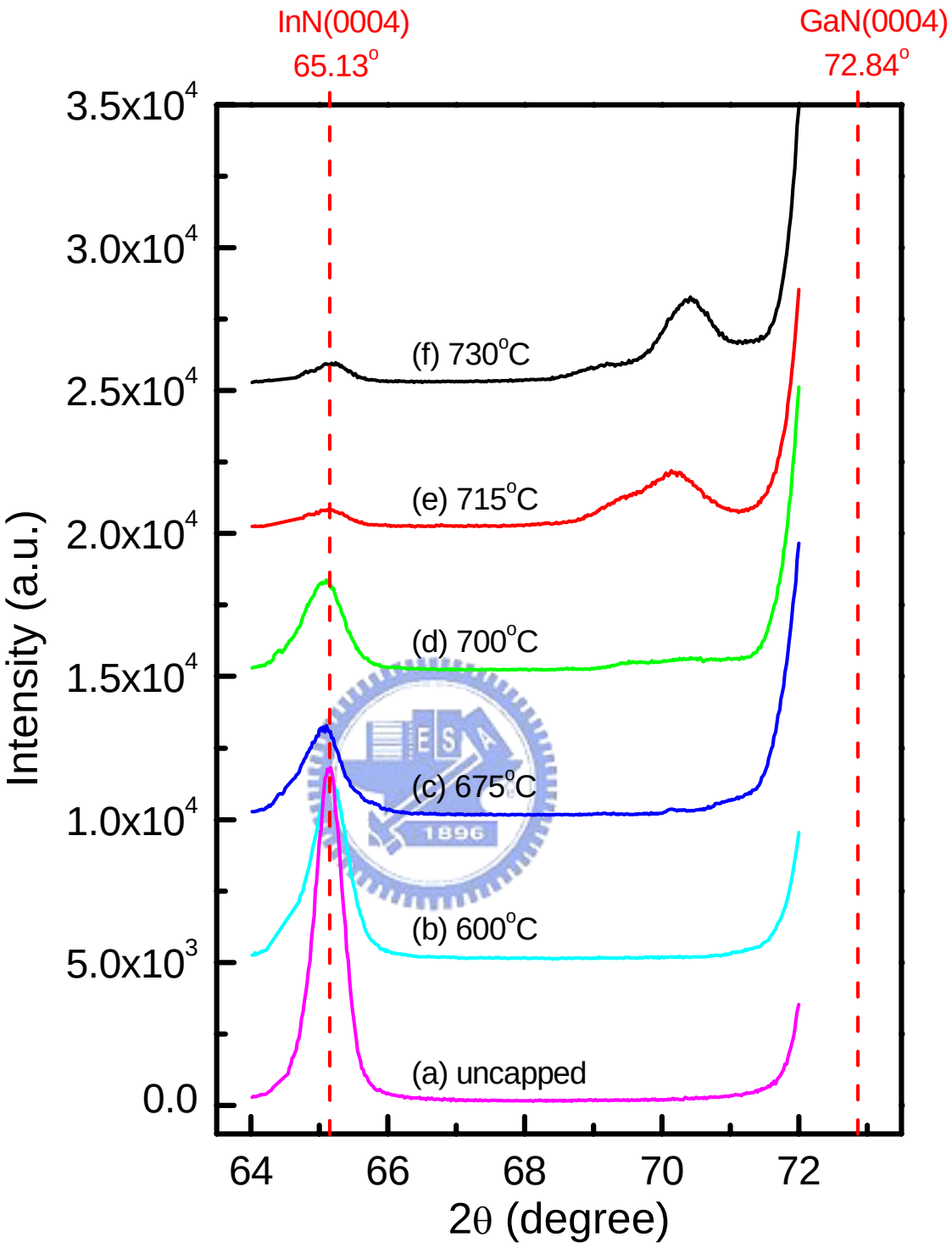

Fig. 4-3-2 The high angle X-ray diffraction curves.

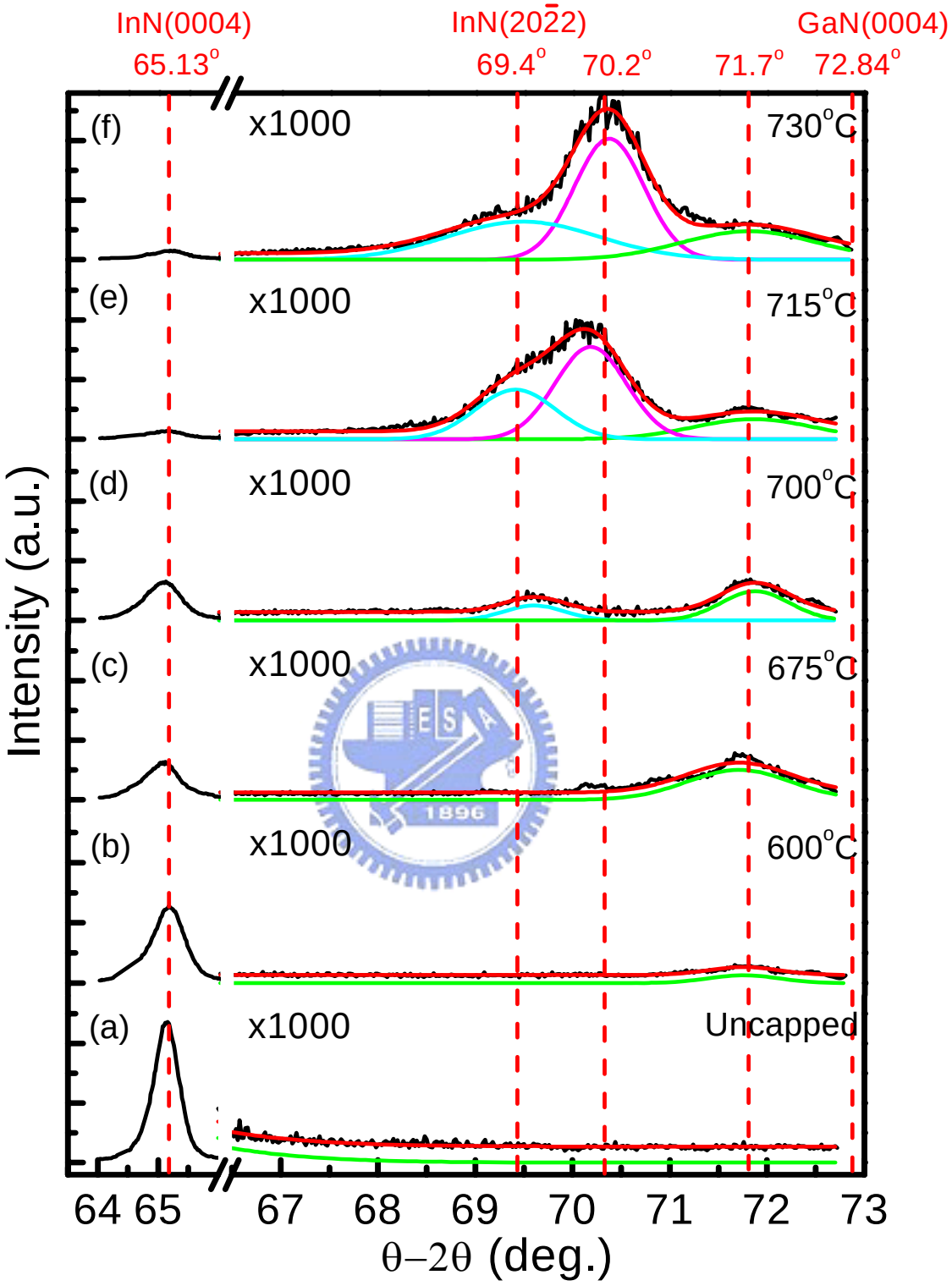

Fig. 4-3-3 The high angle X-ray diffraction curves after subtracting GaN background and the fitting curves.

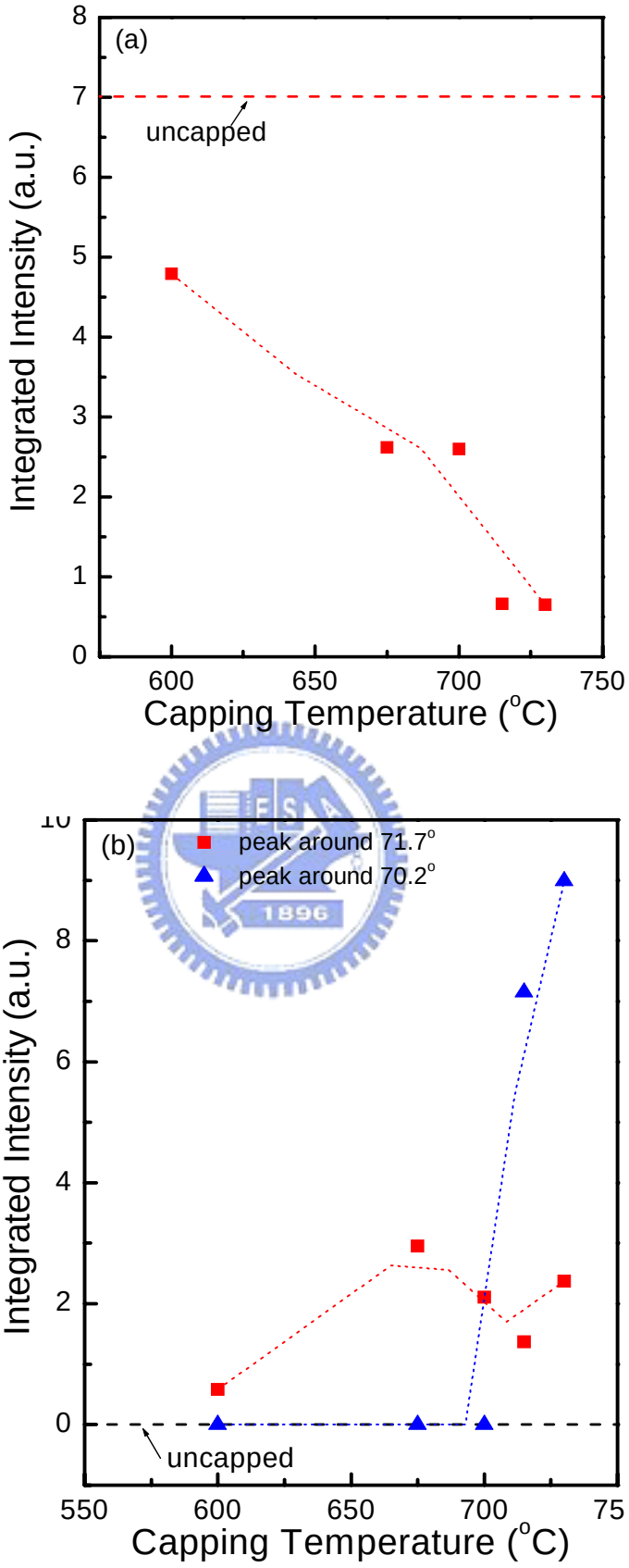

Fig. 4-3-4 The integrated intensity variation of (a) 65.13° InN (004) (b) 71.7° and 70.2° peaks.

4.4 NSOM spectrum on InN nano-dots

With the help of NSOM mapping images, we analyzed the spatial distribution of the visible emission PL signals in this section. Because the NSOM was operated at room temperature the peak position of PL signals have some red shift. The 2.975eV and 2.370eV which above mentioned correspond to around 430nm and 530nm in this section. From both the topographies and NSOM mapping images, we can tell where these 430nm and 530nm visible emission signals are originated. If they had the same spatial distribution, they may be due to the similar (or the same) origin. If not, it maybe due to surface morphology or composition variation in the sample systems. Nevertheless, NSOM mapping images provide important information for studying these visible emission PL peaks in detail.

Fig. 4-4-1 showed the NSOM topographies and mapping images taken at room temperature (300K) of the sample *f* (730℃ capping). Image (a) showed the mapping at 364nm of GaN PL peak. We notice that the V-defect region gives strong PL signals, and other regions are relatively weaker. From the cross-sectional profile of V-defect, its depth was around 100nm which was deeper than InN nano-dots and capping layer. Thus, it is likely that the 364nm emission in V-defect regions was from GaN buffer layer grown at high temperature.

Fig. 4-4-1 (b) and (c) showed the mapping images at 430nm. In image (b), we can see that 430nm emission signal was mainly from the region outside of

InN nano-dots. In image (c), we also see that the 430nm emission signal is not from the region of V-defect.

Fig. 4-4-1 (d) showed the mapping image at 530nm. We did not observe any conspicuous correlation between topography and PL signals, and the 530nm green signals seem to occur from all regions.

In next section we would propose a reasonable model to explain these phenomena observed by NSOM.

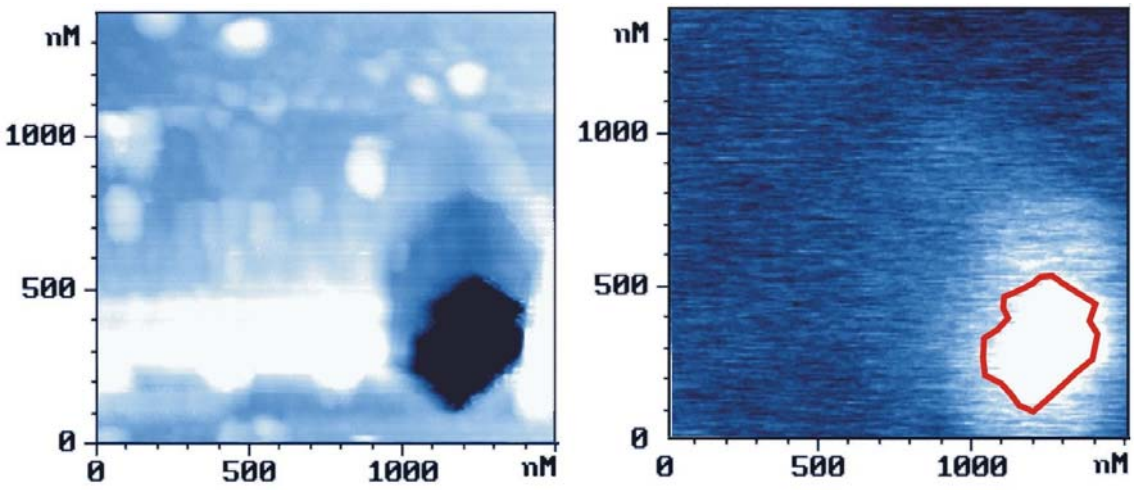

(a) NSOM mapping at 364nm.

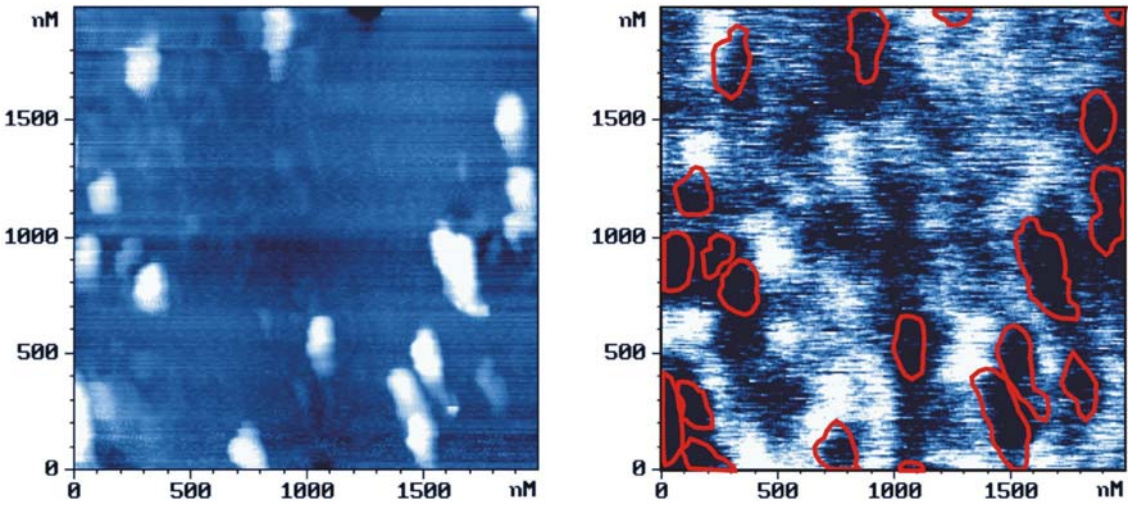

(b) NSOM mapping at 430nm.

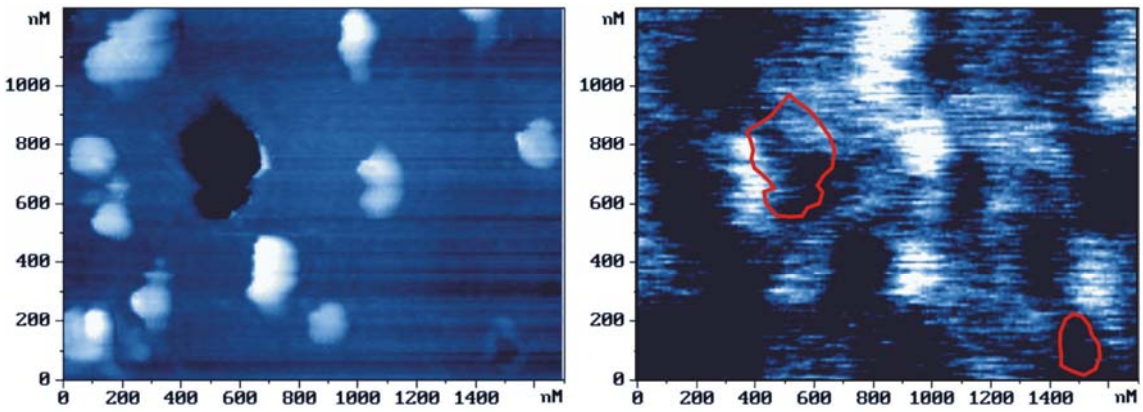

(c) NSOM mapping at 430nm (V-defect).

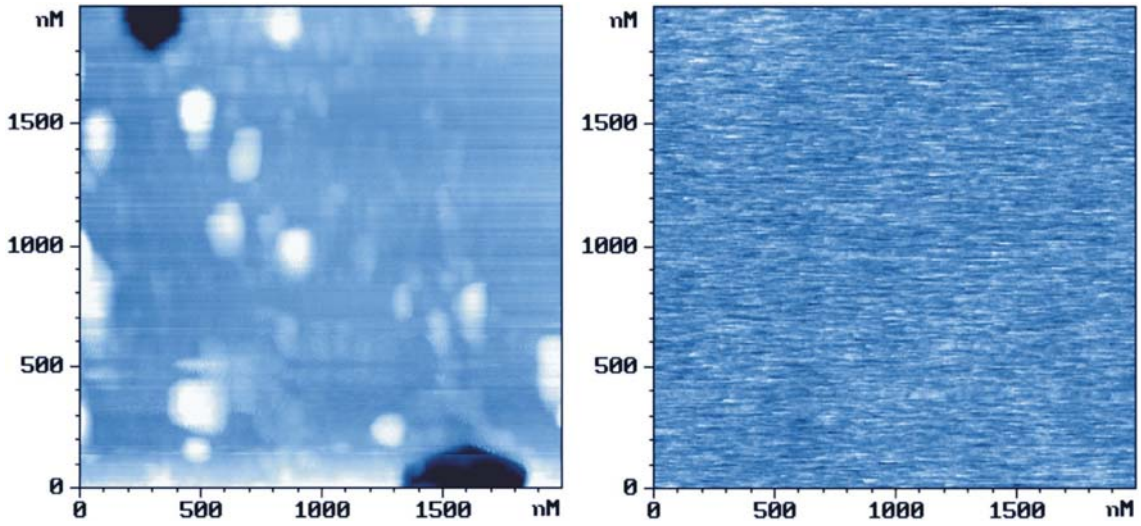

(d) NSOM mapping at 530nm.

Fig. 4-4-1 NSOM topographies and mapping images taken at 300K of sample f (capped 730℃) at (a) 364nm, (b) 430nm, (c) 430nm (V-defect), and (d) 530nm.

4.5 Transition models of visible emission bands

In previous sections, we observed some interesting visible emissions in PL spectra of GaN capped InN nano-dots. By analyzing X-ray diffraction curves, it is revealed that the visible emissions may be due to InGaN formation from the capping effect. We also studied the spatial distribution of the emissions by NSOM mapping, which let us further understand the study. In this section, we will propose different schemes to explain the phenomena observed in NSOM images.

To account for the mapping image showed in Fig. 4-4-1 (a), (Fig. 4-5-1 (a)) we showed the GaN NBE emission (364nm) that is concentrated on the V-shape pit (V-defect). In the other regions, the emission would be absorbed by the interface layer which has either lower bandgap energy or many nonradiative recombination centers. Therefore, the GaN emission (364nm) mainly originates from GaN buffer layer. Because the V-defect region easily extends into the HT-GaN buffer layer, the 364nm emission can come out with little difficult and be collected by the NSOM tip.

For the mapping images of the violet (430nm) emission in Fig. 4-4-1 (b) and (c) we showed the schematic in Fig. 4-5-1 (b) in which PL emission comes from the interface layer that may include InGaN formed by capping (section 4-3). However, much weak emission was observed on InN nano-dots. Since its bandgap energy is the lowest (0.77eV), the violet emission can be reabsorbed. Moreover, there is no PL emission in the V-defect region because it penetrates

the interface layer into HT-GaN region.

Because Fig. 4-4-1 (d) showed the green (530nm) emission rather uniformly we believe that it is from the GaN capping layer. Even on the InN nano-dots, we can still observe this green emission not like the violet emission. If the green emission occurs at the interface layer, it should also be reabsorbed in those nano-dots. However, the PL green emission mapping did not show such a spatial distribution. Therefore, we propose its emission scheme in Fig. 4-5-1 (c).

In summary, we believe that the violet (430nm) PL emission can be attributed to the interface layer between InN nano-dots and GaN buffer layer and the green (530nm) PL emission is from the GaN capping layer. In addition, we checked the PL emission of GaN grown at 700℃ that clearly showed no PL signals. Thus, the GaN NBE emission (364nm) can only come from high temperature grown GaN buffer layer. It is because GaN quality at the capping temperature is too low to give PL emissions.

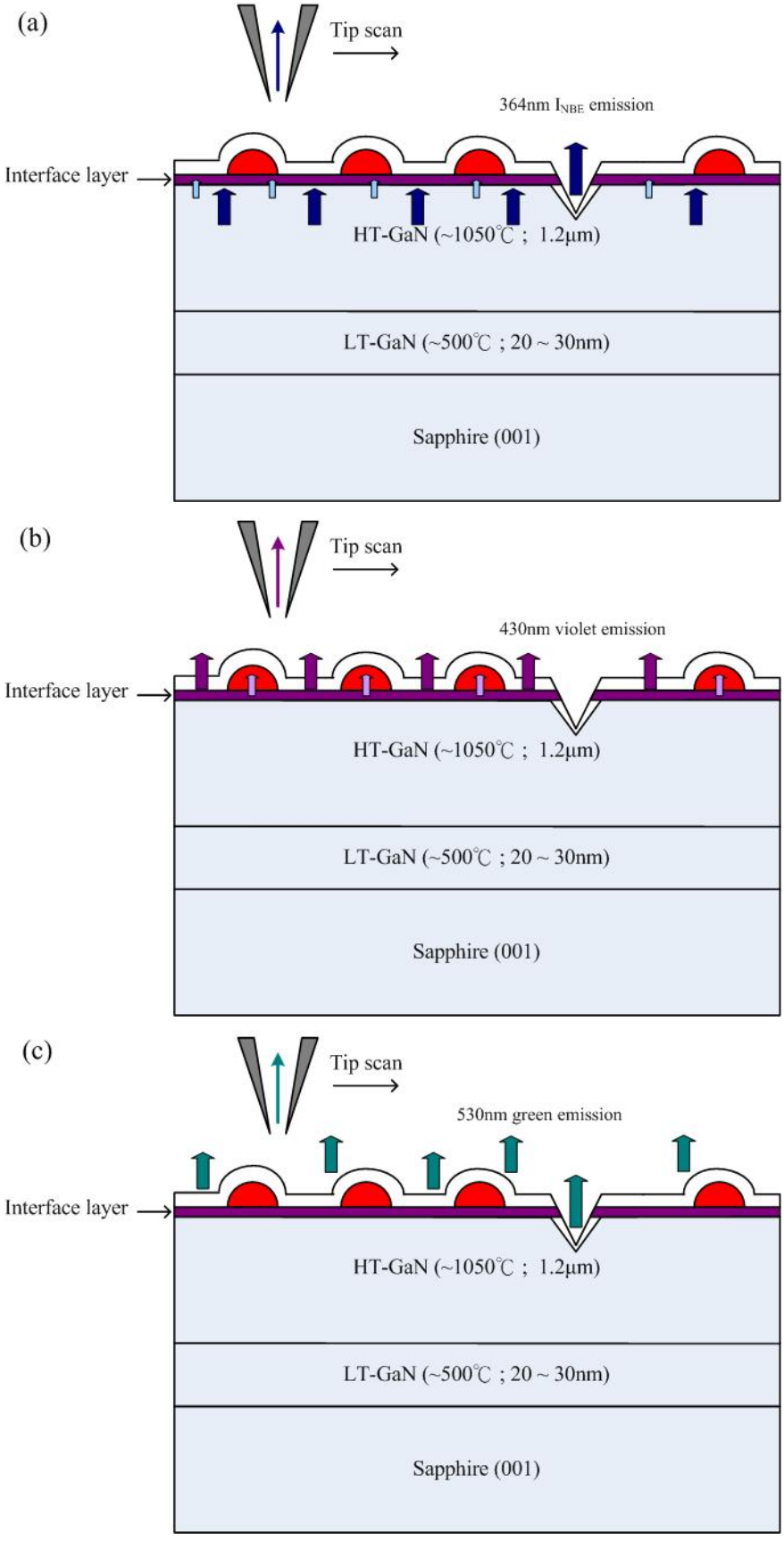

Fig. 4-5-1 the model of (a) GaN NBE (364nm) emission, (b) violet (430nm) emission, (c) green (530nm) emission.

Chapter 5 Conclusions

Capping effect is one important part in InN dots growth process by influencing the dot quality and optical properties. The key factor of the process is the capping temperature. If it occurs at an appropriate temperature, the carriers would be confined in dots and results in good optical properties.

In this thesis, we investigated the capping effects on InN nano-dots. We study the surface morphology by AFM, the composition variation by X-ray diffraction, and the optical properties by PL spectra and NSOM mapping. From AFM images, we clearly observed the deformed profiles of InN nano-dots by increasing the capping temperature. The InN band to band emission appeared at 0.77eV for uncapped sample. The InN emission intensity decreased after capping that seems to be supported by AFM images. Moreover, two extra visible emission bands were observed in PL spectra that were unexpected. By analyzing the X-ray diffraction results, the visible emissions are likely due to the InGaN formation from capping processes. The spatial distribution of NSOM mapping revealed the origins of PL emission bands. Finally, we proposed different schemes to explain the observations in NSOM images. We believe that the visible emissions are from the capping layer and the interface layer between InN nano-dots and GaN layer. The presence of the interface layer may include InGaN formed by capping processes.

The detailed interaction between InN nano-dots and GaN capping layer is worth further studying. Base on this study, we understand that the growth

temperature is critical in optical properties of InN dots and important for improving sample quality.

Reference :

[1] S. Nakamura, M. Senoh, and T. Mukai, *Jpn. J. Appl. Phys.*, Part 2 **32**, L8 (1993).

[2] S. Nakamura, M. Senoh, S. Nagahama, N. Iwasa, T. Yamada, T. Matsushita, H. Kiuoku, and Y. Sugimoto, *Jpn. J. Appl. Phys*. Part2 **35**, L74 (1996).

[3] A. Yamamoto, M. Tsujino, M. Ohkubo, and A. Hashimoto, *Sol. Energy Mater. Sol. Cells* **35**, 53 (1994).

[4] Ashraful Ghani Bhuiyan, Alihiro Hashimoto, and Akio Yamamoto, *Journal of Applied Physics* **94**, 2779 (2003).

[5] J. Wu, W. Walukiewicz, K. M. Yu, J. W. Ager III, E. E. Haller, H. Lu, W. J. Schaff, Y. Saito, and Y. Nanishi, *Appl. Phys. Lett.* **80**, 3967 (2002).

[6] W. R. Runyan and T. J. Shaffner, "Semiconductor Measurements and Instrumentation", second edition, The McGraw-Hill companies, (1998).

[7] Julia W.P. Hsu, *Materials Science and Engineering*, **33** (2001).

[8] K. Kornitzer, T. Ebner, K. Thonke, R. Sauer, C. Kirchner, V. Schwegler, M. Kamp, M. Leszczynski, I. Grzegory, and S. Porowski, *Physical Review B*, **60** (1999).

[9] V. Yu. Davydov, A. A. Klochikhin, R. P. Seisyan, V. V. Emtsev, S. V. Ivanov, F. Bechstedt, J. Furthmuller, H. Harima, A. V. Mudryi, J. Aderhold, O. Semchinova, and J. Graul, Pyhs. *Stat. Sol.* (b), **229** (20002).

[10] Takashi, Matsuoka, Hiroshi, Harima, Eiji Kurimoto, *Applied Physics Leters*, **81**(2002).

[11] T. L. Tansley and C. P. Foley, *J. Appl. Phys*. **59** (1986).

[12] Sukit Limpijumnong, Chris G. Van de Walle, *Physical Review B*, **69** (2004).

[13] Michael A. Reshchikov and Hadis Morkoc, *Journal of Applied Physics*, **97** (2005).

[14] Jorg Neugebauer and Chris G. Van de Walle, *Appl. Pyhs. Lett.*, **69** (1996).

[15] Wright. A. F., Nelson, J. S., *Phys. Rev. B: Condens. Matter*, **51,** 7866 (1995).

[16] Yeh, C. et al., *Phys. Rev. B: Condens. Matter*, **46**, 10086 (1992).

[17] Christensen, N.E., Gorczyca, I., *Phys. Rev. B: Condens. Matter*, **50**, 4397 (1994).

[18] Chen, X. L. et al., *Mod. Phys. Lett. B*, **13**, 285 (1999).

[19] Chen, X. L. et al., *Chin. Phys. Lett.*, **16**, 107 (1999).

[20] Balkas, C., Basceri, C., Davis, R., *Powder Diffraction*, **10**, 266 (1995).

[21] Hiroyuki Shinoka, Nobuki Mutsukura, *Thin Solid Films*, **503**, 8-12 (2006).

[22] M. F. Wu, S. Q. Zhou, A. Vantomme, Y. Huang, H. Wang, and H. Yang, *J. Vac. Sci. Technol. A*, Vol. **24**, No. 2 (2006).

[23] N. A. El-Masry, E. L. Piner, S. X. Liu, and S. M. Bedair, *Appl. Phys. Lett.*, **72** (1998).